



## OPEN

## SUBJECT AREAS:

PHASE TRANSITIONS  
AND CRITICAL  
PHENOMENA

NANOPARTICLES

FLUID DYNAMICS

NONLINEAR PHENOMENA

# Femtosecond Laser Pulse Driven Melting in Gold Nanorod Aqueous Colloidal Suspension: Identification of a Transition from Stretched to Exponential Kinetics

Yuelin Li<sup>1</sup>, Zhang Jiang<sup>1</sup>, Xiao-Min Lin<sup>2</sup>, Haidan Wen<sup>1</sup>, Donald A. Walko<sup>1</sup>, Sanket A. Deshmukh<sup>2</sup>, Ram Subbaraman<sup>3</sup>, Subramanian K. R. S. Sankaranarayanan<sup>2</sup>, Stephen K. Gray<sup>2</sup> & Phay Ho<sup>1</sup><sup>1</sup>Advanced Photon Source, Argonne National Laboratory, 9700 South Cass Ave., Argonne, IL 60439, <sup>2</sup>Center for Nanoscale Materials, Argonne National Laboratory, 9700 South Cass Ave., Argonne, IL 60439, <sup>3</sup>Materials Science Division, Argonne National Laboratory, 9700 South Cass Ave., Argonne, IL 60439.

Received

26 August 2014

Accepted

19 November 2014

Published

30 January 2015

Correspondence and requests for materials should be addressed to Y.L. (ylli@aps.anl.gov) or S.K.R.S.S. (ssankaranarayanan@anl.gov)

Many potential industrial, medical, and environmental applications of metal nanorods rely on the physics and resultant kinetics and dynamics of the interaction of these particles with light. We report a surprising kinetics transition in the global melting of femtosecond laser-driven gold nanorod aqueous colloidal suspension. At low laser intensity, the melting exhibits a stretched exponential kinetics, which abruptly transforms into a compressed exponential kinetics when the laser intensity is raised. It is found the relative formation and reduction rate of intermediate shapes play a key role in the transition. Supported by both molecular dynamics simulations and a kinetic model, the behavior is traced back to the persistent heterogeneous nature of the shape dependence of the energy uptake, dissipation and melting of individual nanoparticles. These results could have significant implications for various applications such as water purification and electrolytes for energy storage that involve heat transport between metal nanorod ensembles and surrounding solvents.

Interaction with light is at the heart in a plethora of nanoparticle applications including drug delivery and photo-induced thermotherapy<sup>1,2</sup>, high capacity data storage<sup>3–5</sup>, chemical and biological sensors<sup>6,7</sup>, solar energy harvesting<sup>8</sup>, and water purification<sup>9</sup>. For nanorods, interaction of a single particle under well controlled condition has been well studied<sup>10</sup>, yet the ensemble behavior of nanorods with random orientations, such as in an aqueous colloidal suspension, can be complicated<sup>11–13</sup> due to the geometrical anisotropy of individual nanorods that lead to heterogeneous response to light excitation. Such anisotropic response normally results in complex, heterogeneous system behavior that is also encountered in human behavior<sup>14</sup>, ecosystem response to climate change<sup>15</sup>, protein folding/unfolding<sup>16</sup>, random fields<sup>17</sup>, anomalous diffusion<sup>18</sup>, and jammed systems<sup>19</sup>, to name a few. An increase or loss of heterogeneity often results in a corresponding change in system dynamics and kinetics, sometimes manifested as a transition from a stretched to a compressed exponential behavior or vice versa<sup>20,21</sup>.

In this paper, we report the experimental finding of a transition from stretched to compressed melting kinetics in an aqueous gold nanorod colloidal suspension driven by femtosecond laser pulses. Detailed analysis and large scale molecular dynamics (MD) simulations elucidate the origin of the observed cross-over kinetics, highlighting the interplay between nanoscale hydrodynamics and heat transfer between nanorod and their surrounding environment.

In the experiments, we use *in situ* small angle X-ray scattering (SAXS)<sup>22</sup> for the measurement of the rod-to-sphere morphological transformation of the nanoparticles. The SAXS spectrum intensity at any wave vector  $Q$  is the sum of the contributions of all types of particles in the ensemble,

$$I(Q) = \sum_{k=1}^K s_k(Q)n_k. \quad (1)$$

Here  $n_k$  is the fractional population of each component,  $\sum_{k=1}^K n_k = 1$ , and  $k$  is the shape index. In this case, index  $k = 1$  represents nanospheres;  $k = K$  represents the starting shape, i.e., nanorods; and intermediate values 1

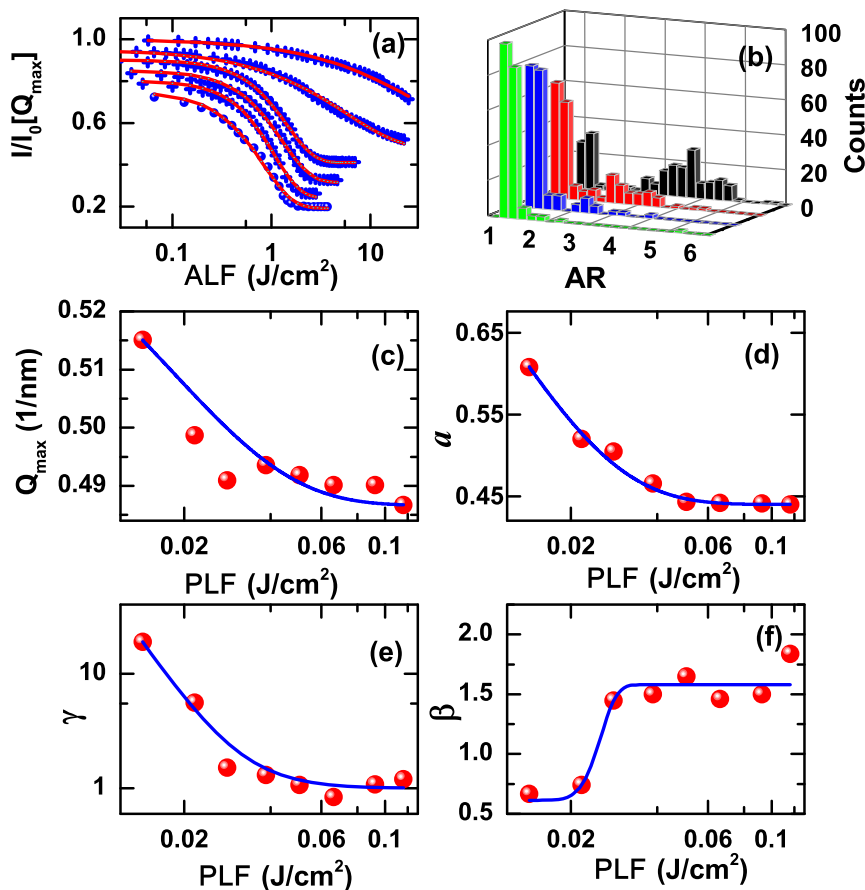


**Figure 1** | (a) The normalized intensity  $I/I_0[Q_{\max}]$  as a function of the total fluence at different peak fluences, top to bottom 14, 21, 28, 38, 50, 66 mJ/cm<sup>2</sup>, with corresponding total number of pulses of 1008, 1000, 504, 120, 56, and 56, respectively. It shows the transition from stretched to compressed exponential. Symbols: measurement. Lines: fit to a stretched exponential in Eq. (2). For examples of raw data, see the SI Fig. S2. (b) Aspect ratio histograms of data extracted from *ex situ* TEM images, before laser exposure (black) and at PLF = 14 (red), 28 (blue), and 116 (green) mJ/cm<sup>2</sup>, showing the drift of the aspect ratio as a function peak fluence. More details of the data are given in SI Fig. S5. (c)  $Q_{\max}$ , and (d–f) parameters  $a$ ,  $\gamma$ , and  $\beta$  in the stretched exponential fitting of the  $I/I_0[Q_{\max}]$  as a function of PLF. Both  $Q_{\max}$  and  $a$  are indications of the final melting states of the ensemble. The abrupt change of the  $\beta$  from below 1 to above 1 indicates the change of the global melting kinetics from a stretched to a compressed exponential. Lines in (c–f) are guides to eye.

$< k < K$  represent spheroids with increasing aspect ratios (AR), respectively. A scattering factor  $s_k(Q)$  is associated with each particle shape. As there is no long-range order in the dilute solution, the summation is linear over all the particles in the ensemble.

A series of melting experiments were performed at different peak laser fluences. Aqueous colloidal suspension of nanorods 45–60 nm long and AR of 3–4.5 in a were exposed to laser pulses with peak fluence ranging from 14 to 116 mJ/cm<sup>2</sup>, with an accumulated laser fluence (ALF or total fluence) in each sample of up to 20 J/cm<sup>2</sup>. Note that, it is the purpose to study the ensemble change as the laser melting progresses and from which we extract the statistics. In this mode of experiment, it is not our intention to keep the initial condition constant. Rather, we wish to examine the melting kinetics as ever more energy (or successive laser pulses) is input into the nanorod samples. We allowed enough time, 2–3 seconds, between the laser exposures (pulses) for the system to relax and mix. The final samples were examined by *ex situ* transmission electron microscopy (TEM). Consistent with previous studies, no fragmentation of the nanorods was observed over the range of peak fluences investigated<sup>11</sup>.

The SAXS data and their corresponding TEM statistics (Figs. 1(a) and (b)) show a clear dependence of the final particle distribution on the peak fluence. The normalized SAXS spectrum intensity,  $I/I_0[Q]$ , represents the SAXS spectrum after laser irradiation normalized to that before irradiation. We further denote

the normalized intensity as  $I/I_0[Q_{\max}]$  at  $Q_{\max}$  where the maximum reduction of  $I/I_0$  is observed. Note that this  $Q_{\max}$  does not necessarily reflect any particular characteristic length from the particles, but rather a location where the rod scattering of a given sample makes a dominant contribution.

The evolution of the scattering intensity  $I/I_0[Q_{\max}]$  as a function of total fluence at each peak fluence fits well to a stretched exponential form (Fig. 1(a)),

$$I(ALF) = a + (1 - a) \exp \left[ - \left( \frac{ALF}{\gamma} \right)^\beta \right], \quad (2)$$

where the fitting parameter  $a$  is a constant offset and  $\beta$  is the dimensionless stretching exponent, essentially measuring the speed of the melting.  $\gamma$ , in units of fluence, sets the scale of total fluence necessary for global melting of the ensemble. They are all found to be a function of the peak fluence (Figs. 1(c–f)).

The  $Q_{\max}$  and  $a$  dependences on the peak fluence (Fig. 1(c–d)) can be explained by the final mean AR reached by the ensemble, and correlate well with our SAXS simulation for mixtures of nanorods and spheroids with different AR (see Supplementary Information (SI) Fig. S1 and the *ex situ* TEM examination of the samples, SI Fig. S3): At high peak fluence, the centroid of the AR for the remaining nanorods is lower, thus lowering  $Q_{\max}$  and decreasing the remaining scattering signal  $a$  at  $Q_{\max}$ .

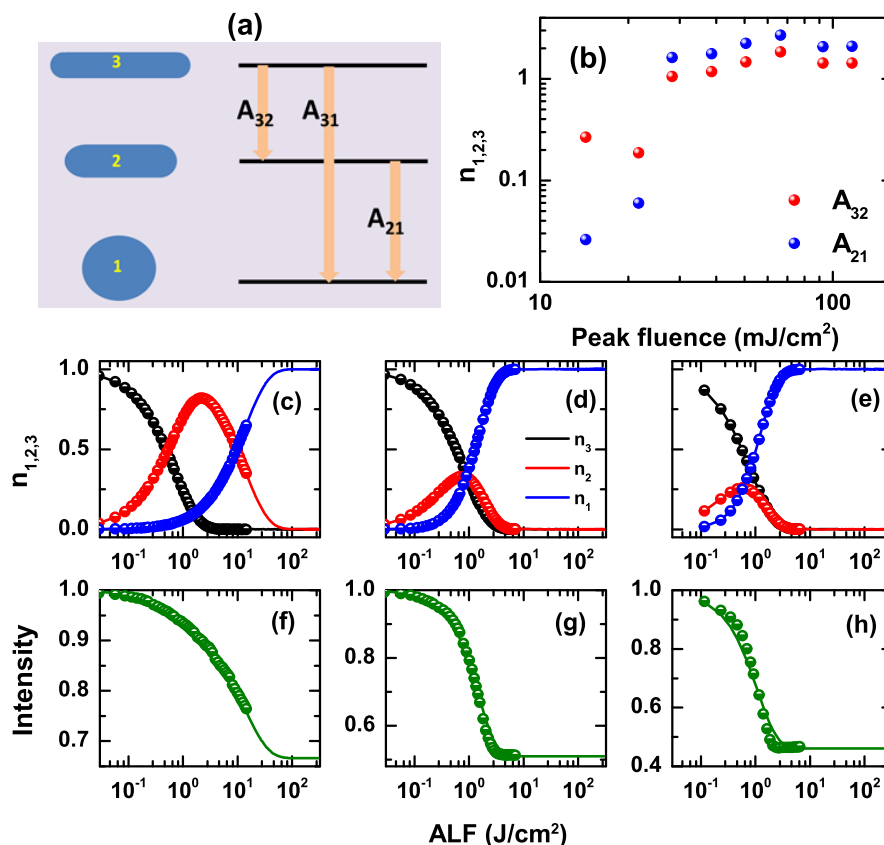


**Figure 2** | (a) A three shape-melting kinetic diagram showing the shape transformation rates from nanorod to nanospheroids and on to nanospheres; (b) Shape transformation rates as a function of peak fluence extracted by fitting the experimentally measured  $I/I_0[Q_{\max}]$  using the three shape model. (c–e) The underlying population shift among the shapes showing the role of the intermediate shape, for peak fluences of 14, 28, and 116  $\text{mJ}/\text{cm}^2$  respectively. At low peak fluence the intermediate shape is long lived, while at high peak fluence the ensemble becomes a bimodal distribution dominated by the original rods and the final spheres. (f–h) The fitting (lines) of the experiment measurement reproduces the SAXS signal (symbols) as function of accumulated fluence, with the same peak fluences as (c–e) respectively.

As the peak fluence increases,  $\gamma$  decreases and reaches a stable value of about 1  $\text{J}/\text{cm}^2$  for peak fluences above 21  $\text{mJ}/\text{cm}^2$  (Fig. 1(e)). The abrupt change of  $\beta$  from about 0.6 to about 1.6 (Fig. 1(f)) indicates a change in the melting kinetics. We note that Link et al. have measured exponential melting kinetics of nanorod using optical absorption spectroscopy<sup>13</sup> while the present SAXS measurement shows the global morphology state.

To quantify this ensemble melting kinetics, we described the melting of each population using a set of rate equations as

$$\frac{dn_k}{dALF} = \sum_{j=k+1}^K A_{jk}n_j - \sum_{j=1}^{k-1} A_{kj}n_k, \quad (3)$$

where  $A_{jk}$  is the melting rate from shape  $j$  into shape  $k$ . Equations (1) and (3) encapsulate the multitude of all possible shape transformations and their effects on the scattering signal. For simplicity, we consider a three-shape system with  $K = 3$ , of which a schematic is depicted in Fig. 2(a). It should be noted that a two-shape model only generates an exponential kinetics and a four or more shape model does not improve the results significantly.

The model is used to fit the measured normalized SAXS spectral intensity. We assign  $s_3 = 1$ ,  $s_1 = 0$ , and  $s_2 = 0.6$ , representing the scattering contribution the initial nanorods, nanospheres, and the intermediate shapes, respectively. The assignment is empirically based on the experiment data and Irena modelling and is relative to monodisperse nanorods, see Figs S1 (b, d), S3 and S4 in the SI. For the intermediate shapes, we have tried values from 0.3 to 0.7, and the fitting in Figure 2 does not seem to be very sensitive to this number. The fitting solves Eq. (3) and minimizes the difference between the

calculated scattering intensity using Eq. (1) and the measured  $I/I_0[Q_{\max}]$  by adjusting the shape transition rates  $A_{jk}$ . The fitting quantitatively reproduced the experimentally measured scattering intensity as a function of ALF (Figs. 2(f–h)). The fitting also qualitatively reproduced the overall morphological shifts of the ensemble (Fig. 2(c–e)) when compared with the TEM analysis, see Fig. 1(b) and SI Fig. S5. The transition rates extracted are given in Fig. 2(b) as a function of the peak fluence.

For the low peak fluence case in Fig. 2(c, f), the intermediate shape represents a long-lived state, with a small  $A_{32}$  and  $A_{21} \ll A_{32}$  shown in Fig. 2(b) when exponent  $\beta < 1$  (Fig. 1(f)). However, as the peak fluence increases, there is an abrupt reversal of the relative magnitude, i.e.,  $A_{21} > A_{32}$  at peak fluence between 21 and 28  $\text{mJ}/\text{cm}^2$  (Fig. 2(b)), corresponding to the prompt change in  $\beta$  from below 1 to larger than 1 in Fig. 1(f). As a result, the system is never dominated by the  $k = 2$  transitional shape (shown in Fig. 2(d, e)), and effectively maintains a bimodal distribution. The relative formation and destruction rates of the intermediate state play key roles in determining the global melting kinetics.

There are several dynamic processes that influence the melting of an individual nanorod, including energy deposition, energy dissipation, and the actual melting. The shift of the relative sensitivity of the melting process to these factors dictates the relative kinetics of formation and destruction of the intermediate shape.

The energy deposition process is dominated by the surface plasmon resonance (SPR) effect. Electrodynamics calculations show that our nanorods have a strong SPR peak at 800 nm when the rods' long axis is aligned to the polarization of the laser field and drops dra-

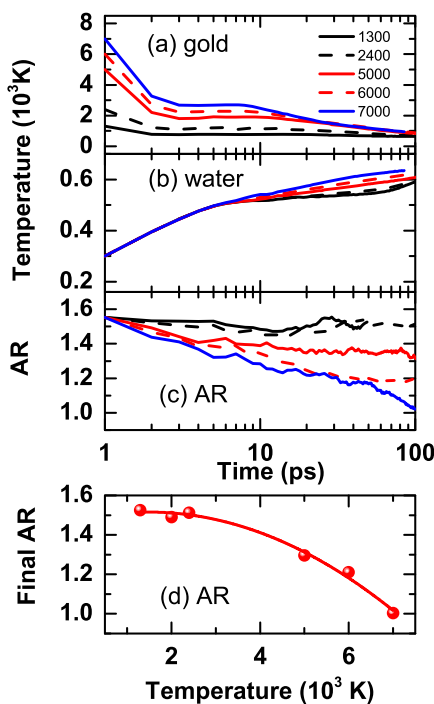


**Figure 3** | MD simulation-based evolution of (a) gold temperature, (b) water temperature, and (c) AR for nanorods with an initial aspect ratio of AR = 1.5. (d) The final AR as a function of the initial temperature, for starting temperatures from 1300 K to 7000 K. In all cases, the surrounding water is initially at room temperature.

matically as the orientation deviates from the laser polarization (SI Fig. S6). Relative to the laser pulse duration, individual nanorods can be considered to be “frozen” in the suspension with random orientation during each laser exposure due to the millisecond rotational timescale of the nanorods<sup>23</sup>.

The anisotropic SPR leads to individual nanoparticles being heated to varied peak temperatures as determined by their instantaneous orientation. At low laser fluence, this leads to a heterogeneous, partial shape transform dominated by surface melting<sup>24</sup>. As these nanorods partially melt, they become less resonant with the SPR and more difficult to heat and melt by subsequent laser exposures, thus establishing an effective energy barrier for the global melting as the population of the partially melted nanorods builds up. The presence of such long-lived intermediate states slows down the melting of the ensemble, leading to a stretched exponential decay as has been observed in folding and unfolding of proteins<sup>16,25,26</sup>.

At high enough peak laser fluence, all the particles in the laser field can be heated to high temperature regardless of the SPR effect. However, since the time it takes for shape transformation is longer for a droplet with higher AR<sup>27</sup>, energy dissipation starts to play an important role, exacerbated by cooling enhanced by the curvature effect at nano scale<sup>28</sup>. This may lead to an intermediate shape formation rate that is lower than its destruction rate, thus compressed exponential kinetics.

To systematically explore the complex interplay between these different effects, we performed a series of self-consistent, multi-million atom MD simulations. Simulations at a constant temperature of 2400 K show that it indeed takes a longer time for the shape of a nanorod with larger AR to transform into a sphere (SI Fig. S7). In addition, upon removing water, the melting time becomes 10 times shorter, highlighting the cooling effect at the gold-water interface.

In the first set of self-consistent simulations, we subject a nanorod with AR = 1.5 to different starting temperatures. The nanoparticle temperature drops rapidly within 30 ps, accompanied by a rapid

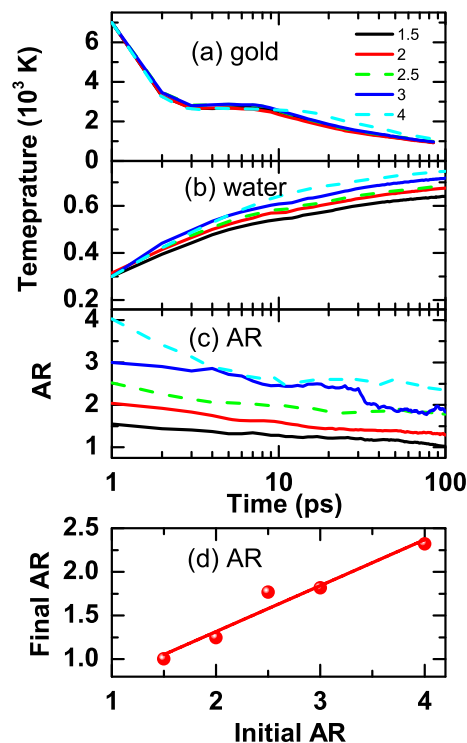


**Figure 4** | MD simulation-based evolution of (a) gold temperature, (b) water temperature, and (c) AR for nanorods initially heated to 7000 K. (d) The final AR as a function of the initial aspect ratio. The volume of the nanorod was kept the same in all the cases.

heating of the water (Figs. 3(a) and (b)). After 100 ps, the nanorods settle either to an intermediate state (for  $T \sim 5000$ – $6000$  K) or transform completely to a sphere ( $T \sim 7000$  K), summarized in Fig. 3(c) and (d). We note, in all cases (even heating to 7000 K), the gold nanorod is cooled within 30 ps to below the gold melting point (1337 K). The continuing shape transformation can be understood as the evolution of a super-cooled liquid while releasing the latent heat<sup>29</sup>.

Figure 4 shows a set of simulations for gold nanorods with various ARs at the same initial temperature of 7000 K. Irrespective of the initial AR, the nanorods are rapidly quenched to temperatures below their melting point after about 20 ps (Fig. 4(a)). Though the gold temperature is about the same for all ARs, water is clearly heated to higher temperature at larger ARs due to the larger surface area (Fig. 4(b)). In all cases, the shape of the nanorod continues to evolve at temperatures below the melting point (Fig. 4(c)). The final ARs at 150 ps are summarized in Fig. 4(d) and show a strong dependence on the initial AR: while the larger AR ( $>2$ ) rods remain as rods with a smaller AR, the rods with smaller AR ( $<1.5$ ) become spheres. This indicated that it may take multiple exposures for the longer rods to reach the nominal intermediate shape but only one exposure to melt the intermediate shape into a sphere. This result clearly establishes a situation where a formation rate is slower than the destruction rate for the intermediate shape at high laser fluence.

The above MD simulations are consistent with the kinetics revealed by our 3-shape model. The 3-shape model suggests that the stretched to compressed exponential crossover occurs between a peak fluence of 20 mJ/cm<sup>2</sup> to 30 mJ/cm<sup>2</sup>, a jump of 1.5 times in fluence. Although it is difficult to directly compare the experimental laser fluence to the MD temperature, the MD simulation in Fig. 3 shows roughly the same ratio of 1.4 between the full melting temperature (7000 K) and partial melting temperature (5000 K) for the intermediate AR = 1.5 nanorods.



It is worth noting that the practical implications of this observed transition on the heat transport rates across the nanorod-solvent interface are significant. For the same volume, the transition from a rod with  $AR = 4$  to a rod with  $AR = 1.5$  leads to a 20% reduction in surface area (see SI). For a given heat input to the nanorod, this suggests that the rate of heat transfer would decrease by  $\sim 10\%$  as the cross-over from stretched to compressed exponential kinetics takes place. Such a change is significant in applications such as water-purification<sup>9</sup> where the goal is to maximize heat transport from the nanorods to the water. Similarly, a reduced efficiency of heat transport is detrimental for energy storage applications utilizing high thermal conductivity nanorods for efficient heat dissipation from the electrolytes. Our study thus provides operational guidelines for applications involving such nanorod colloidal suspensions.

Though it is tempting to corroborate the simulation of different particles into the experiment control, our samples always include a distribution of aspect ratios (ARs), and therefore it is difficult to directly corroborate the simulations for specific AR ratios. Even with a relatively monodisperse sample, after the first laser pulse the monodispersity will be compromised. In general, we find a complex dependence of the melting dynamics of the particles on the orientation, laser fluence, and shape. However, the simulation does provide important insight into the mechanism behind the observed kinetics.

To conclude, the observed crossover from stretched to compressed exponential kinetics signifies a dramatic shift in the underlying system heterogeneity. The complex kinetics is mediated by the creation and destruction of the intermediate shapes that serve as heating/melting barriers in the multiplicative melting process associated with the morphology transformation. These complex behaviors originate from the heterogeneous dynamics of individual nanorods in energy uptake, heat dissipation, and melting. Our observation clearly illustrates the physical pathway of the transition of the dynamics which may be important for the applications of such metal nanorods as well as understanding other complex systems consisting of units with shifting heterogeneous response to external excitations.

## Methods

Gold nanorods were synthesized using a seed mediated growth procedure, slightly modified from the procedure published in the literature<sup>30</sup>. First, spherical gold seed nanoparticles were produced by adding 0.6 mL of freshly made, ice/water-cooled  $\text{NaBH}_4$  (10 mM) to a 10 mL aqueous solution containing 0.1 M CTAB and 0.25 mM  $\text{HAuCl}_4$ . Next, a growth solution was prepared as follows: 7.5 mL of 10 mM  $\text{HAuCl}_4$  and 0.45 mL  $\text{AgNO}_3$  with a fixed concentration were mixed with 150 mL of 0.1 M CTAB, the solution was acidified with 3 mL of 1 M HCl, and Au(III) was then reduced to Au(0) by the addition of 1.2 mL of 0.1 M L-ascorbic acid. After 5 min of aging, 0.36 mL of the gold-seed solution was added to the growth solution. The temperature of the growth reaction was maintained at 30°C for about 3 h. The as-prepared sample was centrifuged once at 8100 rpm for 30 min. The supernatant was removed, and the nanorod sample was re-dispersed in water at higher concentration for a better signal-to-noise ratio for the x-ray measurement. The average size of the gold nanorods in the sample is 10–20 nm in diameter and 45–60 nm in length. Optical absorption spectroscopy revealed a strong resonance at about 800 nm.

The melting experiment was performed at 7-ID-C at the Advanced Photon Source<sup>31</sup>. Linearly polarized laser pulses of 800 nm wavelength and 50 fs duration were focused to a 1.7 mm by 1.5 mm spot (full width at half maximum) to illuminate the sample. SAXS spectra after each laser exposure were recorded on a PILATUS 100 k detector and then azimuthally integrated to obtain the profile of scattering intensity as a function of scattering angle. The sample was held in 1-mm diameter fused silica capillaries with a section length of about 1 mm, or a volume of 78.5  $\mu\text{L}$ . The estimated variation of the sample volume is  $\pm 20\%$  considering the variation in the diameter of the capillaries. The sample was condensed to a concentration of about  $2.8 \times 10^{13}/\text{mL}$  to enhance the signal-to-noise ratio. The average distance between the nanorods is about 400 nm and thus collective effects can be ignored.

Large-scale multi-million atom molecular dynamics simulations were performed to explore the melting of gold nanorods in water. The potential model for gold, water and gold-water interactions are given in the SI (Table S1). A gold nanorod was placed in a simulation cell and was relaxed, in vacuum at 300 K, under NVT ensembles for 100 ps. Temperature was controlled using a Nose-hoover thermostat with time constants of 1 ps. The relaxation of gold nanorod was followed by random insertion of SPC/Fw water molecules. The initial water density was chosen to be close to bulk water  $\sim 1$  g/mL. This system with gold nanorod and water was further relaxed for 200 ps at 300 K under NPT ensembles. Several systematic simulations were conducted, on the relaxed gold nanorod and water system, under NVE ensemble. The

effect of temperature on the melting of gold nanorods was studied by simulating gold-nanorods with different starting temperatures from 1300 K to 7000 K. We have also simulated gold nanorods with different aspect ratios with starting temperature fixed at 7000 K. Noting that our particle is still smaller than those in the experiment, a comparison of particle with different size is also performed with no significant difference (SI Fig. S8). The initial temperature of the water is kept constant at 300 K. Table S2 lists the gold nanorods simulated in this work. Simulations were conducted for up to 200 ps and the atomic trajectories (atom positions, temperature, pressure, velocities etc.) were accumulated and stored every 1 ps. The LAMMPS simulation package was used to carry out all the simulations with periodic boundary conditions with LJ cut-off of 10.0 Å for non-bonded interactions<sup>32</sup>. Trajectories obtained from the simulations were extracted to explore the structural evolution of the rod, the density variation of the surrounding water, and the temperature profiles of gold nanorods and water molecules.

Our electrostatics calculations employed the discrete dipole approximation (DDA)<sup>33,34</sup> and utilized the gold refractive index data of Johnson and Christy<sup>35</sup>.

- Dreaden, E. C., Alkilany, A. M., Huang, X., Murphy, C. J. & El-Sayed, M. A. The golden age: gold nanoparticles for biomedicine. *Chem. Soc. Rev.* **41**, 2740 (2012).
- Bardhan, R., Lal, S., Joshi, A. & Halas, N. J. Theranostic Nanoshells: From Probe Design to Imaging and Treatment of Cancer. *Acc. Chem. Res.* **44**, 936–946 (2011).
- Zijlstra, P., Chon, J. W. M. & Gu, M. Five-dimensional optical recording mediated by surface plasmons in gold nanorods. *Nature* **459**, 410–413 (2009).
- Ullah, M. A. et al. Low energy-density recording with a high-repetition-rate laser beam in gold-nanorod-embedded discs. *Opt. Express* **20**, 24516 (2012).
- Li, X., Lan, T.-H., Tien, C.-H. & Gu, M. Three-dimensional orientation-unlimited polarization encryption by a single optically configured vectorial beam. *Nat. Commun.* **3**, 998 (2012).
- Anker, J. N. et al. Biosensing with plasmonic nanosensors. *Nat. Mater.* **7**, 442–453 (2008).
- Kabashin, A. V. et al. Plasmonic nanorod metamaterials for biosensing. *Nat. Mater.* **8**, 867–871 (2009).
- Atwater, H. A. & Polman, A. Plasmonics for improved photovoltaic devices. *Nat. Mater.* **9**, 205–213 (2010).
- Neumann, O. et al. Compact solar autoclave based on steam generation using broadband light-harvesting nanoparticles. *Proc. Natl. Acad. Sci.* **110**, 11677–11681 (2013).
- Zijlstra, P., Chon, J. W. M. & Gu, M. White light scattering spectroscopy and electron microscopy of laser induced melting in single gold nanorods. *Phys. Chem. Chem. Phys.* **11**, 5915 (2009).
- Link, S., Burda, C., Nikoobakht, B. & El-Sayed, M. A. Laser-Induced Shape Changes of Colloidal Gold Nanorods Using Femtosecond and Nanosecond Laser Pulses. *J. Phys. Chem. B* **104**, 6152–6163 (2000).
- Link, S., Wang, Z. L. & El-Sayed, M. A. How Does a Gold Nanorod Melt? *J. Phys. Chem. B* **104**, 7867–7870 (2000).
- Link, S. & El-Sayed, M. A. Spectroscopic determination of the melting energy of a gold nanorod. *J. Chem. Phys.* **114**, 2362 (2001).
- Gomez, B. T., Wilson, J. M. & Ryzhkov, S. I. Political Sophistication and Economic Voting in the American Electorate: A Theory of Heterogeneous Attribution. *Am. J. Polit. Sci.* **45**, 899–914 (2001).
- Post, E. et al. Ecological Dynamics Across the Arctic Associated with Recent Climate Change. *Science* **325**, 1355–1358 (2009).
- Udgaonkar, J. B. Multiple Routes and Structural Heterogeneity in Protein Folding. *Annu. Rev. Biophys.* **37**, 489–510 (2008).
- Young, A. P. *Spin glasses and random fields*. (World Scientific, 1998).
- Bouchaud, J.-P. & Georges, A. Anomalous diffusion in disordered media: Statistical mechanisms, models and physical applications. *Phys. Rep.* **195**, 127–293 (1990).
- Biroli, G. Jamming: A new kind of phase transition? *Nat. Phys.* **3**, 222–223 (2007).
- Falus, P., Borthwick, M., Narayanan, S., Sandy, A. & Mochrie, S. Crossover from Stretched to Compressed Exponential Relaxations in a Polymer-Based Sponge Phase. *Phys. Rev. Lett.* **97**, 066102 (2006).
- Ballesta, P., Duri, A. & Cipelletti, L. Unexpected drop of dynamical heterogeneities in colloidal suspensions approaching the jamming transition. *Nat. Phys.* **4**, 550–554 (2008).
- Walter, G., Kranold, R., Gerber, T., Baldrian, J. & Steinhart, M. Particle size distribution from small-angle X-ray scattering data. *J. Appl. Crystallogr.* **18**, 205–213 (1985).
- Zijlstra, P., van Stee, M., Verhart, N., Gu, Z. & Orrit, M. Rotational diffusion and alignment of short gold nanorods in an external electric field. *Phys. Chem. Chem. Phys.* **14**, 4584 (2012).
- Inasawa, S., Sugiyama, M. & Yamaguchi, Y. Laser-Induced Shape Transformation of Gold Nanoparticles below the Melting Point: The Effect of Surface Melting. *J. Phys. Chem. B* **109**, 3104–3111 (2005).
- Ihalainen, J. A. et al.  $\alpha$ -Helix folding in the presence of structural constraints. *Proc. Natl. Acad. Sci.* **105**, 9588–9593 (2008).
- Sułkowska, J. I., Noel, J. K. & Jose, N. Onuchic. Energy landscape of knotted protein folding. *Proc. Natl. Acad. Sci.* **109**, 17789–17794 (2012).
- Cohen, A. & Carriere, C. J. Analysis of a retraction mechanism for imbedded polymeric fibers. *Rheol. Acta* **28**, 223–232 (1989).



28. Merabia, S., Shenogin, S., Joly, L., Keblinski, P. & Barrat, J.-L. Heat transfer from nanoparticles: A corresponding state analysis. *Proc. Natl. Acad. Sci.* **106**, 15113–15118 (2009).
29. Wang, Q., Liu, C. T., Yang, Y., Dong, Y. D. & Lu, J. Atomic-Scale Structural Evolution and Stability of Supercooled Liquid of a Zr-Based Bulk Metallic Glass. *Phys. Rev. Lett.* **106**, 215505 (2011).
30. Nikoobakht, B. & El-Sayed, M. A. Preparation and Growth Mechanism of Gold Nanorods (NRs) Using Seed-Mediated Growth Method. *Chem. Mater.* **15**, 1957–1962 (2003).
31. Dufresne, E. M. *et al.* Time-Resolved Research at the Advanced Photon Source Beamline 7-ID. in *AIP Conference Proceedings* **1234**, 181–184 (2010).
32. Plimpton, S. Fast Parallel Algorithms for Short-Range Molecular Dynamics. *J. Comput. Phys.* **117**, 1–19 (1995).
33. Draine, B. T. & Flatau, P. J. Discrete-dipole approximation for scattering calculations. *J. Opt. Soc. Am. A* **11**, 1491 (1994).
34. Draine, B. T. & Flatau, P. J. User Guide for the Discrete Dipole Approximation Code DDSCAT 7.3. *ArXiv Prepr. ArXiv13056497* (2013).
35. Johnson, P. B. & Christy, R. W. Optical Constants of the Noble Metals. *Phys. Rev. B* **6**, 4370–4379 (1972).

## Acknowledgments

This work was performed, in part, at the Advanced Photon Source, the Center for Nanoscale Materials, and Argonne Leadership Computing Facility, all U.S. Department of Energy, Office of Science, Office of Basic Energy Sciences User Facilities, under Contract No.

DE-AC02-06CH11357. The authors thank Jan Ilavsky and Byeongdu Lee for insightful discussion and Harold Gibson for technical help.

## Author contributions

Y.L. conceived and designed the experiment; S.K.R.S.S. guided the MD simulation, X.L. prepared the samples; Y.L., Z.J., H.W. and D.W. performed the experiments. P.H., R.S., S.D., S.S. and S.G. performed the MD and DDA calculations. Y.L. and S.K.R.S.S. wrote the paper.

## Additional information

**Supplementary information** accompanies this paper at <http://www.nature.com/scientificreports>

**Competing financial interests:** The authors declare no competing financial interests.

**How to cite this article:** Li, Y. *et al.* Femtosecond Laser Pulse Driven Melting in Gold Nanorod Aqueous Colloidal Suspension: Identification of a Transition from Stretched to Exponential Kinetics. *Sci. Rep.* **5**, 8146; DOI:10.1038/srep08146 (2015).



This work is licensed under a Creative Commons Attribution-NonCommercial-NoDerivs 4.0 International License. The images or other third party material in this article are included in the article's Creative Commons license, unless indicated otherwise in the credit line; if the material is not included under the Creative Commons license, users will need to obtain permission from the license holder in order to reproduce the material. To view a copy of this license, visit <http://creativecommons.org/licenses/by-nc-nd/4.0/>